

RSC Advances



This is an *Accepted Manuscript*, which has been through the Royal Society of Chemistry peer review process and has been accepted for publication.

Accepted Manuscripts are published online shortly after acceptance, before technical editing, formatting and proof reading. Using this free service, authors can make their results available to the community, in citable form, before we publish the edited article. This *Accepted Manuscript* will be replaced by the edited, formatted and paginated article as soon as this is available.

You can find more information about *Accepted Manuscripts* in the [Information for Authors](#).

Please note that technical editing may introduce minor changes to the text and/or graphics, which may alter content. The journal's standard [Terms & Conditions](#) and the [Ethical guidelines](#) still apply. In no event shall the Royal Society of Chemistry be held responsible for any errors or omissions in this *Accepted Manuscript* or any consequences arising from the use of any information it contains.

Enhanced supercapacitor performance by incorporating nickel in manganese oxide

Preety Ahuja, Sanjeev Kumar Ujjain, Raj Kishore Sharma* and Gurmeet Singh

Department of Chemistry, University of Delhi, Delhi 110 007, INDIA

Abstract

Nickel manganese mixed oxides ($\text{Ni}_y\text{Mn}_{1-y}\text{O}_x$; $0 \leq y \leq 0.4$) has been synthesized by in-situ inclusion of nickel during the growth of manganese oxide (MnO_x). Effect of nickel concentration in MnO_x is investigated by Cyclic Voltammetry, Current-Voltage characteristics, Scanning Electron Microscopy and N_2 adsorption-desorption analysis. Variation in electronic conductivity and specific capacitance suggest that nickel concentration in MnO_x matrix significantly affect the supercapacitor electrode performance. At Ni/Mn ~ 0.25 i.e. $\text{Ni}_{0.2}\text{Mn}_{0.8}\text{O}_x$, material crystallizes into spinel NiMn_2O_4 as prominent phase and exhibited specific surface area ($118 \text{ m}^2\text{g}^{-1}$) with granular morphology. Furthermore $\text{Ni}_{0.2}\text{Mn}_{0.8}\text{O}_x$ exhibited low resistivity ($2.07 \times 10^4 \text{ ohm cm}$) and consequently high specific capacitance $\sim 380 \text{ Fg}^{-1}$, endowing additional merits. Fabricated supercapacitor device ($\text{Ni}_{0.2}\text{Mn}_{0.8}\text{O}_x/\text{Ni}_{0.2}\text{Mn}_{0.8}\text{O}_x$), deliver 35 Wh Kg^{-1} energy density and 3.74 kW Kg^{-1} power density with remarkably high capacitive retention $\sim 92 \%$ after 3000 galvanostatic charge/discharge cycles. These encouraging results show great potential in developing energy storage device from manganese oxide based electrodes incorporating nickel in lattice.

Keywords

Nickel manganese mixed oxide, supercapacitor, specific capacitance, energy density

Corresponding Author: Dr. Raj K. Sharma, Email drrajksharma@yahoo.co.in,
FAX: 91-11-27666646 Ext 156

1. INTRODUCTION

Electrochemical supercapacitors have attracted much attention as energy storage device due to their promising applications in portable electronics and hybrid electrical vehicles [1,2]. Supercapacitors store charge via (a) charge accumulation at the electrode/electrolyte interface in the form of electrical double layer (EDL) and (b) by the pseudocapacitance that arises from faradic redox transitions that go deep inside the bulk material.

Carbon materials store charge via EDL whereas transition metal oxides and conducting polymers follow redox process for charge storage [3,4]. EDL is surface dependent and therefore the resulting capacitance values are low however the charge discharge rates are high. Due to the bulk contribution, pseudocapacitors give high specific capacitance (C_{SP}) whereas the response time limits their application. In order to exploit high C_{SP} and energy density, metal oxides have been extensively studied and the response time or charge/discharge time is modified by improving the charge collection through a support material, preferably carbon. Researchers recently focussed on mixed metal oxides as potential supercapacitor electrode materials because pristine transition metal oxides are poor conductors resulting in high equivalent series resistance with limited capacity and power density [5]. Besides good electronic conduction, mixed transition metal oxides could offer richer redox reactions beneficial for electrochemical applications [6].

Recently, many nanocomposites like $\text{Co}_3\text{O}_4 @\text{MnO}_2$, $\text{Co}_3\text{O}_4\text{-Ni(OH)}_2$, $\text{MnO}_2\text{-NiO}$ are attracting great interest for supercapacitors owing to their improved traits over pristine counterparts [7-12]. Various Nickel and Cobalt composites result in high electronic conductivity consequently enhancing the electrochemical performance [11]. Liu et al.

synthesized high surface area spinel nickel manganese oxide for supercapacitor with high C_{SP} 243 Fg^{-1} at $5mVs^{-1}$. Fan et al. reported MnO_2 -NiO nanoflake-assembled tubular array on stainless steel substrate by template method where ZnO is employed as in situ sacrificial template [9]. Although high capacitance values are achieved using nano architectures, the bulk material performance and the electrode cyclability could be further improved.

In this work, we investigated the in situ inclusion of nickel in Manganese oxide ($Ni_yMn_{1-y}O_x$; $0 \leq y \leq 0.4$) lattice and tested the composite material as supercapacitor electrodes. $NiMn_2O_4$ crystallizes as a prominent phase when 20 wt% $NiCl_2$ is added to 80 wt% aqueous $MnCl_2$ solution for oxidative growth of manganese oxide. $Ni_{0.2}Mn_{0.8}O_x$ exhibits highest electrical conductivity and surface area among other compositions. Proposed supercapacitor, $Ni_{0.2}Mn_{0.8}O_x/Ni_{0.2}Mn_{0.8}O_x$ provides high energy density $35 WhKg^{-1}$ with $\sim 92\%$ retention of initial C_{SP} after 3000 galvanostatic charge/discharge cycles.

2. EXPERIMENTAL

2.1 Materials. Nickel chloride ($NiCl_2 \cdot 6H_2O$), Manganese chloride ($MnCl_2 \cdot 4H_2O$), Sodium hydroxide (NaOH), Sodium sulphate (Na_2SO_4), isopropyl alcohol (IPA) and isooctane were purchased from Merck. Perfluorinated ion exchange resin (Nafion) was procured by Sigma Aldrich. Sodium sulphosuccinate (AOT) was used as surfactant (supplied by Alfa Aesar).

2.2 Synthesis of Nickel Manganese mixed oxide. Three aliquots of reverse microemulsions of water/AOT/isooctane [13] were prepared having 0.8 M $MnCl_2$, 0.2 M $NiCl_2$ and 2 M NaOH aqueous solutions respectively. These were thoroughly mixed in a reaction vessel and stirred for 2 hr. Excessive volume of IPA was added to break the micellar arrangement after completion of the reaction. The resulting precipitate was collected after washing several

times with IPA and deionized water. Solid product obtained after washing was dried overnight at 80°C. Different compositions of $\text{Ni}_y\text{Mn}_{1-y}\text{O}_x$; $0.1 \leq y \leq 0.4$ were prepared as given in Table 1 (y is molar concentration of nickel in MnO_x). MnO_x and $\text{Ni}(\text{OH})_2$ were also synthesized by the same method under similar conditions [14].

2.3 Preparation of electrode. 10 mg of composite material ($\text{Ni}_y\text{Mn}_{1-y}\text{O}_x$; $0.1 \leq y \leq 0.4$) was ultrasonically mixed with 5 wt % Nafion in IPA. The mixture after 30 min. sonication was spray deposited on 1 cm^2 area of the polished graphite sheets (2 x 1cm) with the help of N_2 gas. After spray deposition, the film was dried at 80°C in air and weighed to estimate the loading of the composite material. Loading was found to be approximately 0.3 mg cm^{-2} .

2.4 Characterization. Conductivity measurements were carried out on pellet (dia. 10 mm) using Keithley 2400 source meter. Perkin Elmer model 1257 X-ray Photoelectron spectroscope (XPS) was employed to estimate the percentages of different metal oxide phases present in the specimen. Powder X-Ray Diffraction (XRD) measurements were performed with Bruker D8 Advance X-ray diffractometer. Microstructural investigations were carried out using Zeiss Ultra 55 Field emission scanning electron microscope (FESEM). Surface area of the samples were analyzed by N_2 adsorption desorption isotherms using Micromeritics ASAP-2020. High resolution transmission electron microscopy (HRTEM) and Selected Area Electron Diffraction (SAED) was conducted on Phillips Technai T-300 microscope. Electrochemical tests were performed with CHI 604D electrochemical analyzer. A piece of platinum gauze and Ag/AgCl were assembled as the counter and reference electrode respectively. Polished graphite with metal oxide/mixed metal oxide coating served as the working electrode. Cyclic voltammograms (CV) were recorded by polarizing the working electrode between 0 to 0.9V vs Ag/AgCl in 0.5 M aqueous Na_2SO_4 electrolyte. The charge/discharge characteristics of the supercapacitor cell were evaluated at different current

density (two electrode assembly) using an Arbin instrument (model: BT2000, USA). C_{SP} was calculated from galvanostatic charge/discharge curve according to following equation [3,15]:

$$C = \frac{I\Delta t}{m\Delta V}$$

where I is the current, $\Delta V/\Delta t$ is the change in potential with time and m is mass loading on the electrode.

The energy density (E in Wh Kg⁻¹) and power density (P in W Kg⁻¹) were expressed as

$$E = \frac{1}{2 \times 3.6} CV^2$$

$$P = \frac{V^2}{4mR}$$

where C is measured device capacitance, m is total mass loading on the electrodes, V is the operating potential range and R is the equivalent series resistance calculated from IR drop in Galvanostatic discharge curve.

3. RESULTS AND DISCUSSION

The effect of Ni incorporation in MnO_x matrix was studied using Cyclic Voltammetry (CV) and Current (I)-Voltage (V) characteristics for Ni_yMn_{1-y}O_x; 0.1 ≤ y ≤ 0.4. Figure 1 shows the variation of C_{SP} and electrical resistivity with different nickel percentage in MnO_x. Ni_{0.1}Mn_{0.9}O_x did not show much change in C_{SP} but the resistivity is slightly increased. Ni_{0.2}Mn_{0.8}O_x, compared to MnO_x shows more than twice increase in C_{SP} with drastic decrement in resistivity. Upon 20 wt% inclusion of Ni, C_{SP} of MnO_x (180 Fg⁻¹) remarkably increases to 380 Fg⁻¹ with one order decrease in resistivity (1.85 X 10⁵ ohm cm of MnO_x to

2.07×10^4 ohm cm of $\text{Ni}_{0.2}\text{Mn}_{0.8}\text{O}_x$). With further increase in nickel content, $\text{Ni}_{0.4}\text{Mn}_{0.6}\text{O}_x$ shows detrimental effect as C_{SP} decreases and resistivity increases. More importantly, drastic increment in C_{SP} of $\text{Ni}_{0.2}\text{Mn}_{0.8}\text{O}_x$ is investigated by its structural and electrochemical analysis.

Figure 2 shows scanning electron micrographs and the surface area analysis using BET. The surface microstructure of MnO_x , $\text{Ni}_{0.2}\text{Mn}_{0.8}\text{O}_x$ and $\text{Ni}_{0.4}\text{Mn}_{0.6}\text{O}_x$ exhibit granular morphology. MnO_x in Figure 2a, shows aggregated spherical grains of dia. ~ 10 nm. $\text{Ni}_{0.2}\text{Mn}_{0.8}\text{O}_x$ exhibited an increase in grain size (dia. ~ 15 nm) (Figure 2b). Upon increasing Ni concentration to 40 wt % ($\text{Ni}_{0.4}\text{Mn}_{0.6}\text{O}_x$), the composite exhibited dense microstructural features with very high aggregation (Figure 2c). It appears that the increased concentration of Ni increases the aggregation.

N_2 adsorption-desorption isotherm analysis of MnO_x show high specific surface area ($80.5 \text{ m}^2\text{g}^{-1}$) with Type IV isotherm with H1 type hysteresis loop (Figure 2d). Upon inclusion of 20 wt% nickel ($\text{Ni}_{0.2}\text{Mn}_{0.8}\text{O}_x$), surface area significantly increases to $118 \text{ m}^2\text{g}^{-1}$. Nearly 50% enhancement in the specific surface area is attributed due to the complex pore network as in case of H2 hysteresis loop (Figure 2e). Increasing the Ni more than 20 wt%, the surface area shows a decrease (Figure 2f) and is attributed to the dense morphology of the composite having high Ni concentration. Pore size distribution of MnO_x (Suplimentary info S1) demonstrate the presence of mesopores (5-20 nm) whereas in $\text{Ni}_{0.2}\text{Mn}_{0.8}\text{O}_x$, majority of pores fall in the optimal sizes of 2-5 nm for supercapacitors [16] and thus supports the high surface area of $\text{Ni}_{0.2}\text{Mn}_{0.8}\text{O}_x$, consequently resulting in enhanced capacitance.

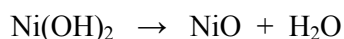
XPS analysis of MnO_x show two peaks of MnO_2 and Mn_3O_4 in Mn 2p at 641.8 eV and 642.43 eV respectively [17]. Areas covered under MnO_2 and Mn_3O_4 peak are estimated

to be 85% and 15% respectively (Figure 3a) ascertaining the simultaneous presence of MnO_2 and Mn_3O_4 in MnO_x . As shown in Figure 3b, the survey scan of $\text{Ni}_{0.2}\text{Mn}_{0.8}\text{O}_x$ confirm the presence of Mn, Ni and O in the composite. Inset shows Ni 2p XPS which is assigned to Ni $2p_{3/2}$ and Ni $2p_{1/2}$ peaks with two satellites (sat.). The spin energy separation of Ni $2p_{3/2}$ and Ni $2p_{1/2}$ is 17.5 eV which is characteristic of $\text{Ni}(\text{OH})_2$ phase [18] Mn 2p XPS spectrum of $\text{Ni}_{0.2}\text{Mn}_{0.8}\text{O}_x$ shows a single peak at 642.4 eV (Figure 3c), analogous to that of MnO_x ascertaining the absence of Mn_3O_4 in $\text{Ni}_{0.2}\text{Mn}_{0.8}\text{O}_x$.

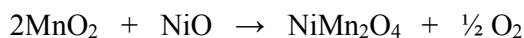
XRD analysis of MnO_x and $\text{Ni}_{0.2}\text{Mn}_{0.8}\text{O}_x$ further supported XPS results. Figure 3d shows XRD patterns of Manganese oxide (MnO_x) and $\text{Ni}_{0.2}\text{Mn}_{0.8}\text{O}_x$. Diffraction pattern of MnO_x endorses the presence of different phases i.e. MnO_2 and Mn_3O_4 [19]. XRD pattern of $\text{Ni}_{0.2}\text{Mn}_{0.8}\text{O}_x$ exhibits three major diffraction peaks at 18° , 35.6° and 63.5° indexed to (111), (311) and (440) planes of spinel NiMn_2O_4 respectively [20, 21]. The diffraction pattern showed relatively amorphous character with indication of the presence of some secondary phases like MnO_2 , $\text{Ni}(\text{OH})_2$ and NiMnO_3 , interestingly there is no sign of Mn_3O_4 . An important observation of the work is that in situ incorporation of 20 wt% Ni in MnO_x results in NiMn_2O_4 as prominent phase formation with complete suppression of manganese higher oxide (Mn_3O_4) phases. The suppression of Mn_3O_4 is attributed to its distorted spinel structure having Mn^{+2} ions in tetrahedral sites and Mn^{+3} ions in octahedral sites [22]. These Mn^{+3} ions causes Jahn Teller distortion which is the result of departure from ideal interactions among bonding orbital and gives rise to lattice instability [23]. Ni^{+2} ions can replace Mn^{+3} ions from octahedral site and such a substitution might require an equivalent amount of remaining Mn^{+3} ions to lose electrons and become Mn^{+4} in order to maintain the charge balance consequently resulting in NiMn_2O_4 . Such a cation distribution offers lesser lattice alterations during electrochemical cycling resulting in enhanced electrochemical stability of NiMn_2O_4 [8].

Annealing carried out at different temperatures helped understanding the growth of NiMn_2O_4 by intermixing of secondary phases. Figure 3e shows diffraction patterns of $\text{Ni}_{0.2}\text{Mn}_{0.8}\text{O}_x$ powder after 2hr annealing at different temperatures. XRD pattern of $\text{Ni}_{0.2}\text{Mn}_{0.8}\text{O}_x$ without any annealing treatment show three major diffraction peaks at 2θ value of 18° , 35.6° , 63.5° confirming the presence of NiMn_2O_4 [24] with some other less intense peaks of MnO_2 , $\text{Ni}(\text{OH})_2$ and NiMnO_3 . Annealing results in grain growth and intermixing of the secondary phases. The $\text{Ni}_{0.2}\text{Mn}_{0.8}\text{O}_x$ sample after 250°C annealing shows the presence of prominent NiMn_2O_4 with some secondary phases of MnO_2 and NiO and a shoulder NiMnO_3 at 36.7° . Here, $\text{Ni}(\text{OH})_2$ converts to NiO which shows a peak at 61.2° corresponding to (220) plane. Further elevation in annealing temperature (450°C) shows the crystalline XRD pattern of NiMn_2O_4 with presence of NiMnO_3 . Quantification of the above XRD pattern by Xpert High Score software via Rietveld method (supplementary information S2) suggest the percentage of prominent phase NiMn_2O_4 (81.3%) and NiMnO_3 (18.7%). It is assumed that the secondary phases of MnO_2 and NiO intermix and form NiMn_2O_4 . The formation of NiMnO_3 could be due to dissociation of NiMn_2O_4 phase as discussed in later section. The XRD pattern of $\text{Ni}_{0.2}\text{Mn}_{0.8}\text{O}_x$ annealed at 650°C made this aspect clear and showed higher (44.5%) percentage of NiMnO_3 [25]. The increase in intensity of the peaks corresponds to gradual evolution to crystalline phases.

Thermo-gravimetric analysis of $\text{Ni}_{0.2}\text{Mn}_{0.8}\text{O}_x$ supports the phase transformation as observed in the X-ray diffraction. Due to loss of the adsorbed and/or structurally bonded water, TGA thermogram of $\text{Ni}_{0.2}\text{Mn}_{0.8}\text{O}_x$ (Figure 3f) shows $\sim 18\%$ weight loss below 120°C . Further weight loss $\sim 7\%$ between $120\text{-}250^\circ\text{C}$ corresponds to the decomposition of $\text{Ni}(\text{OH})_2$ to NiO and H_2O according to the following probable reaction:



Gradual 8% weight loss between 350-450°C is attributed to the formation of NiMn₂O₄ and evolution of oxygen according to the reaction: [26]



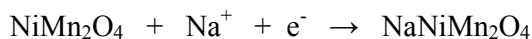
Major 36% weight loss between 450-700°C is attributed to the evaporation of MnO from NiMn₂O₄ according to the following reaction which is in agreement with the XRD results of Ni_{0.2}Mn_{0.8}O_x oxide annealed at 650°C:



As MnO is evaporated, characteristic peaks in the XRD pattern corresponds to NiMn₂O₄ and NiMnO₃ which shows the simultaneous presence of both.

TEM micrographs in Figure 4a shows spherical particles with dia. ~20 nm. Continuous lattice fringes (Figure 4b) reveals d spacing 0.25 nm (311) of NiMn₂O₄. Three different planes (111), (311) and (440) of NiMn₂O₄ are observed in SAED pattern which are in agreement with XRD results (Figure 4c). SEM of Ni_{0.2}Mn_{0.8}O_x (Figure 4d) shows interconnected spherical nanoparticles forming porous channels. EDX results of spherical particles show Ni/Mn ratio ~ 0.25 which is in agreement with experimental value (Figure 4e).

The electrochemical performance of Ni_{0.2}Mn_{0.8}O_x is investigated by Cyclic Voltammetry (CV) and Electrochemical impedance spectroscopy (EIS). CV of Ni_{0.2}Mn_{0.8}O_x show much larger area indicating higher charge storage (~380 Fg⁻¹) than MnO_x (~180 Fg⁻¹) and Ni(OH)₂ (~95 Fg⁻¹), (Figure 5a). This C_{SP} is higher than previous MnO₂-based nanocomposites electrodes, such as the graphene/MnO₂-based textile (315 Fg⁻¹) and MnO₂ nanosheets/graphene (263 Fg⁻¹) [12,27,28]. Moreover, absence of any peak indicates pseudoconstant charging and discharging over whole voltammetric cycle [29]. The possible charge storage mechanism in Ni_{0.2}Mn_{0.8}O_x (NiMn₂O₄ prominent phase) may be explained as:



Complex plane plot of $\text{Ni}_{0.2}\text{Mn}_{0.8}\text{O}_x$ reveals resistive and capacitive response with change in frequency (Figure 5b). The equivalent circuit for the best fit conditions is shown in the inset. High frequency region of the Nyquist plot, represented by suppressed semicircle shows internal resistance R_S 5.3Ω and the high to mid frequency region represents RC circuit (R_{CT} , charge transfer resistance and C_{dl} , double layer capacitance). R_{CT} (1Ω), lower than earlier reported values of MnO_2 -NiO composite indicates intimate contact formation between the current collector and electrolyte contributing to facile charge transfer [9]. A 45° sloped line in the mid frequency range corresponds to Warburg impedance which is related to ion diffusion resistance. Inset shows Nyquist plot of MnO_x and $\text{Ni}_{0.2}\text{Mn}_{0.8}\text{O}_x$ exhibiting similar behaviour in high and low frequency region. Besides, the impedance line of MnO_x possess an arc in mid frequency region restricting the accessibility of ions causing low capacitance of MnO_x . More importantly, capacitive character of $\text{Ni}_{0.2}\text{Mn}_{0.8}\text{O}_x$ attains earlier than that of MnO_x as evident from higher knee frequency below which maximum energy is easily accessible.

Effect of annealing on C_{SP} of $\text{Ni}_{0.2}\text{Mn}_{0.8}\text{O}_x$ is shown by Figure 5c. Inset shows variation of C_{SP} vs annealing temperature. $\text{Ni}_{0.2}\text{Mn}_{0.8}\text{O}_x$ has NiMn_2O_4 as prominent phase which shows high C_{SP} 380 Fg^{-1} . It is important to mention that the samples were dried at 80°C for 1 hr. Extending this temperature to 250°C for 2 hr results in C_{SP} decrement to 290 Fg^{-1} which may be due to improved crystallinity of the material [30]. At 450°C , single phase XRD pattern (NiMn_2O_4) shows C_{SP} 220 Fg^{-1} which is in close proximity to the reported values [12]. Above 450°C , crystalline evolution takes place and the crystal lattice is rigid and not easily expanded (or contracted). This consequently retards the protonation (or deprotonation) reaction of the oxide leading to drastic decrement of C_{SP} at 650°C .

Cycling life stability of MnO_x and $\text{Ni}_{0.2}\text{Mn}_{0.8}\text{O}_x$ is explored by relatively long time cycling at 50 mVs^{-1} (Figure 5d). Result shows that C_{SP} of $\text{Ni}_{0.2}\text{Mn}_{0.8}\text{O}_x$ shows an increment in initial cycles followed by ~99% retention up to 10,000 cycles. Initial increment is probably attributed to activation process involving the increment in the number of available active sites allowing the trapped ions to gradually diffuse out [31]. C_{SP} decay in MnO_x decays is found to be 50% after 10,000 cycles. This remarkable difference in cycling life stability with and without nickel in MnO_x electrode is investigated by XPS analysis before and after electrochemical cycling.

Core level Mn 2p XPS of MnO_x after redox cycling (unlike before cycling) shows intense peak of Mn_3O_4 with relatively less intense MnO_2 peak (Figure 5e). $\text{Ni}_{0.2}\text{Mn}_{0.8}\text{O}_x$ after electrochemical cycling shows a single peak of MnO_2 with no Mn_3O_4 . This demonstrate considerable conversion of MnO_2 to less electroactive Mn_3O_4 phase during cycling (Figure 5f). This implicates that the decrement in charge storing capacity of MnO_x was due to the gradual formation of Mn_3O_4 . It is noteworthy that in-situ availability of nickel (20 wt%) in MnO_x inhibits Mn_3O_4 formation not only during growth but also during redox cycling, thereby enhancing the electrochemical performance of $\text{Ni}_{0.2}\text{Mn}_{0.8}\text{O}_x$.

As a demonstration of application potential of $\text{Ni}_{0.2}\text{Mn}_{0.8}\text{O}_x$, a symmetric supercapacitor, $\text{Ni}_{0.2}\text{Mn}_{0.8}\text{O}_x/\text{Ni}_{0.2}\text{Mn}_{0.8}\text{O}_x$ is fabricated and examined via GCD measurements. Figure 6a shows GCD curves of $\text{Ni}_{0.2}\text{Mn}_{0.8}\text{O}_x/\text{Ni}_{0.2}\text{Mn}_{0.8}\text{O}_x$ at different current densities. Deviation from the linear variation of voltage with time is attributed to pseudocapacitive nature of the material. Small IR drop associated with the discharge curve ascertains low equivalent series resistance (esr) of the cell which can be calculated from the slope of linear correlation of IR drop with current density [32, 33].

Variation of C_{SP} and IR drop at different current density in Figure 6b display lesser esr $\sim 0.03 \Omega$ favouring high power delivery in practical applications making it a potential material for supercapacitor. Moreover, C_{SP} decreases with increase of current density as lesser surface area is accessible at higher current densities. It delivers energy density 35 Wh Kg^{-1} with power density 3.74 kW Kg^{-1} at 0.5 Ag^{-1} (Figure 6c). It still maintains an energy density 5.10 Wh Kg^{-1} and power density 7.44 kW Kg^{-1} even at high current density 12.5 Ag^{-1} .

Long term cycling performance of $\text{Ni}_{0.2}\text{Mn}_{0.8}\text{O}_x/\text{Ni}_{0.2}\text{Mn}_{0.8}\text{O}_x$ was investigated by GCD cycling at 2.5 Ag^{-1} (Figure 6d). Inset shows overview of charge /discharge cycles. Slight increment in C_{SP} during initial 1000 cycles as observed in various reports [31], followed by 8% decrement in C_{SP} in further cycles. Such a high retainability of initial C_{SP} after 3000 cycles endows a long term stable material for charge storage in supercapacitor.

4. CONCLUSIONS

In situ inclusion of nickel during manganese oxide ($\text{Ni}_y\text{Mn}_{1-y}\text{O}_x$; $0 \leq y \leq 0.4$) growth and its effect on structural, electrical and electrochemical properties is investigated. Upon 20 wt % addition of nickel in MnO_x ($\text{Ni}_{0.2}\text{Mn}_{0.8}\text{O}_x$) the composite exhibited spinel NiMn_2O_4 as prominent phase with highest surface area ($118 \text{ m}^2\text{g}^{-1}$), Consequently the superior performance in terms of highest conductivity and C_{SP} ($\sim 380 \text{ Fg}^{-1}$). Galvanostatic charge discharge measurements of fabricated supercapacitor, $\text{Ni}_{0.2}\text{Mn}_{0.8}\text{O}_x/\text{Ni}_{0.2}\text{Mn}_{0.8}\text{O}_x$ demonstrate high energy and power density (35 Wh Kg^{-1} , 3.74 kW Kg^{-1}). Furthermore, it also retains 92% initial capacitance after 3000 cycles ascribing excellent cycling stability.

ACKNOWLEDGEMENTS

Authors gratefully acknowledge the financial support from DST India through project SR/S1/PC-31/2010 and Delhi University for Docotoral Research Grant. Preety Ahuja thankfully acknowledges the research fellowship from UGC India. SK Ujjain thank the INSPIRE fellowship from DST. Authors thank Dr. R. Nagarajan, Department of Chemistry, University of Delhi for electrical characterisation instrumentation and Inorganic Materials and Catalysis group for the support through analysis of surface area using N₂ Sorption facility under DST(SR/S1/PC-11/2011).

REFERENCES

1. Z. Li, J. Wang, L. Niu, J. Sun, P. Gong, W. Hong, L. Ma, S. Yang, *J. Power Sources* 2014, 245, 224-231.
2. G. Wang, L. Zhang, J. Zhang, *Chem. Soc. Rev.* 2012, 41, 797-828.
3. S. K. Ujjain, K. Deori, R. K. Sharma, S. Deka, *ACS Appl. Mater. Interfaces* 2013, 5, 10665-10672.
4. P. Simon, Y. Gogotsi, *Nat. Mater* 2008, 7, 845-854.
5. D. L. Fang, B. C. Wu, Y. Yan, A. Q. Mao, C. H. Zheng, *J. Solid State Electrochem.* 2012, 16, 135-142.
6. J. M. Luo, B. Gao, X. G. Zhang, *Mat. Res. Bull* 2008, 43, 1119-1125.
7. J.P. Liu, J. Jiang, C.W. Cheng, H.X. Li, J.X. Zhang, H. Gong, H.J. Fan, *Adv. Mater.* 2011, 22, 2076-2081.
8. C. H. Tang, X. Yin, H. Gong, *ACS Appl. Mater. Interfaces* 2013, 5, 10574-10582.
9. J. Lu, J. Jiang, M. Bosman, H. J. Fan, *J. Mater. Chem*, 2012, 22, 2419-2426.

10. B. Liu, B. Liu, Q. Wang, X. Wang, Q. Xiang, D. Chen, G. Chen, ACS Appl. Mater. Interfaces 2013, 5, 10011-10017.
11. J.H. Zhong, A.L. Wang, G.R. Li, J.W. Wang, Y.N. Ou, Y.X. Tong, J. Mater. Chem. 2012, 22, 5656-5665.
12. M. Zhang, S. Guo, L. Zheng, G. Zhang, Z. Hao, L. Kang, Z. H. Liu, Electrochim. Acta 2013, 87, 546-553.
13. R. K. Sharma, H.S. Oh, Y. G. Shul, H. Kim, J. Power Sources 2007, 173, 1024-1028.
14. D. Liu, B. B. Garcia, Q. Zhang, Q. Guo, Y. Zhang, S. Sepehri, G. Cao, Adv. Funct. Mater. 2009, 19, 1015–1023.
15. P. Ahuja, V. Sahu, S. K. Ujjain, R. K. Sharma, G. Singh, Electrochim. Acta 2014 doi 10.1016/j.electacta.2014.09.039.
16. R. Ding, L. Qi, H. Wang, J. Solid State Electrochem. 2012, 16, 3621-3633.
17. M. Chigane, M. Ishikawa, M. Izaki, J. Electrochem. Soc. 2001, 148, D96-D101.
18. I. C. Chang, T. T. Chen, M. H. Yang, H. T. Chiu, C. Y. Lee, J. Mater. Chem. A 2014, 2, 10370-10374.
19. Y. Z. Zheng, H. Y. Ding, M. L. Zhang, Mat. Res. Bull. 2009, 44, 403-407.
20. Y. Torii, A. Tsuzuki, K. Kato, Y. Uwamino, B.H. Choi, M.J. Lee, J. Mat. Sci. 1996, 31, 2603-2607.
21. Menaka, N. Garg, S. Kumar, D. Kumar, K. V. Ramanujachary, S. E. Lofland, A. K. Ganguli, J. Mater. Chem. 2012, 22, 18447-18453.
22. J.D. Hem, C.J. Lind, C.E. Roberson, Geochim. et. Cosmochim. Acta 1989, 53, 2811-2822.
23. T. N. Ramesh, P. V. Kamath, J. Power Sources 2008, 175, 625-629.
24. Y. Torii, A. Tsuzuki, K. Kato, Y. Uwamino, B. H. Choi, M. J. Lee, Journal of Material Science, 1996, 31, 2603-2607.
25. S. H. Kim, S. J. Kim, J. Kim, Journal of Power Sources, 2006, 163, 294-299.

26. J. D. Hem, C. J. Lind, *Geochimica et Cosmochimica Acta* 1991, 55, 2435-2451.
27. G. H. Yu, L. B. Hu, M. Vosgueritchian, H. L. Wang, X. Xie, J. R. McDonough, X. Cui, Y. Cui and Z. N. Bao, *Nano Lett.*, 2011, 11, 2905-2911.
28. Z. P. Li, J. Q. Wang, X. H. Liu, S. Liu, J. F. Ou and S. R. Yang, *J. Mater. Chem.*, 2011, 21, 3397-3403.
29. X. Lang, A. Hirata, T. Fujita, M. Chen, *Nat. Nanotech.* 2011, 6, 232-236.
30. J. W. Lang, L. B. Kong, W. J. Wu, M. Liu, Y. C. Luo, L. Kang, *J. Solid State Electrochem.* 2009, 13, 333-340.
31. T. Liu, S. Xu, L. Wang, J. Chu, Q. Wang, X. Zhu, N. Bing, P. K. Chu, *J. Mater. Chem.* 2011, 21, 19093-19100.
32. L. F. Chen, Z. H. Huang, H. W. Liang, Q. F. Guan, S. H. Yu, *Adv. Mater.* 2013, 25, 4746-4752.
33. H. Jiang, C. Li, T. Sun, J. Ma, *Chem. Commun.* 2012, 48, 2606-2608.

List of table

Table 1. Percentage of nickel in manganese oxide.

Figure Captions

Figure 1 Effect of Ni (wt%) on resistivity and C_{SP} of $Ni_yMn_{1-y}O_x$; $0 \leq y \leq 0.4$.

Figure 2 SEM micrographs (a, b and c) and N_2 adsorption-desorption isotherms (d, e and f) of MnO_x , $Ni_{0.2}Mn_{0.8}O_x$ and $Ni_{0.4}Mn_{0.6}O_x$.

Figure 3 (a) Mn 2p X-ray photoelectron spectrum (XPS) of MnO_x , (b) XPS survey scan with Ni 2p core level spectra in inset (c) Deconvoluted Mn 2p spectrum of $Ni_{0.2}Mn_{0.8}O_x$, (d) X-ray diffraction patterns of MnO_x and $Ni_{0.2}Mn_{0.8}O_x$, (e) XRD patterns of $Ni_{0.2}Mn_{0.8}O_x$ powder annealed at 250°C, 450°C and 650°C and (f) Thermogravimetric analysis of $Ni_{0.2}Mn_{0.8}O_x$.

Figure 4 (a) TEM of $Ni_{0.2}Mn_{0.8}O_x$ and (b) HRTEM shows d spacing ~ 0.25 nm, (c) SAED pattern, (d) SEM and (e) EDX of $Ni_{0.2}Mn_{0.8}O_x$ with atomic percentage of Ni:Mn ~ 0.25 .

Figure 5 (a) Cyclic Voltammograms (CV) of MnO_x , $Ni(OH)_2$ and $Ni_{0.2}Mn_{0.8}O_x$ at $5mVs^{-1}$, (b) Nyquist plot of $Ni_{0.2}Mn_{0.8}O_x$ in high frequency region. Inset shows Nyquist plot of MnO_x and $Ni_{0.2}Mn_{0.8}O_x$, (c) Effect of annealing temperature on CV response of $Ni_{0.2}Mn_{0.8}O_x$ electrode. Inset shows variation of specific capacitance vs annealed temperatures, (d) Cycling life test of MnO_x and $Ni_{0.2}Mn_{0.8}O_x$ at $50mVs^{-1}$ and (e and f) Mn 2p XPS spectra of $Ni_{0.2}Mn_{0.8}O_x$ and MnO_x after 10,000 CV cycles.

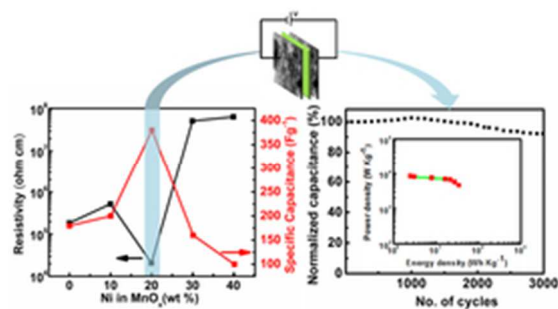
Figure 6 (a) Galvanostatic charge discharge (GCD) curves at different current densities, (b) Variation of IR drop and specific capacitance vs current density, (c) Ragone plot and (d) GCD cycling performance of $Ni_{0.2}Mn_{0.8}O_x//Ni_{0.2}Mn_{0.8}O_x$ supercapacitor cell. Inset shows overview of last cycles.

Table 1. Percentage of nickel in manganese oxide

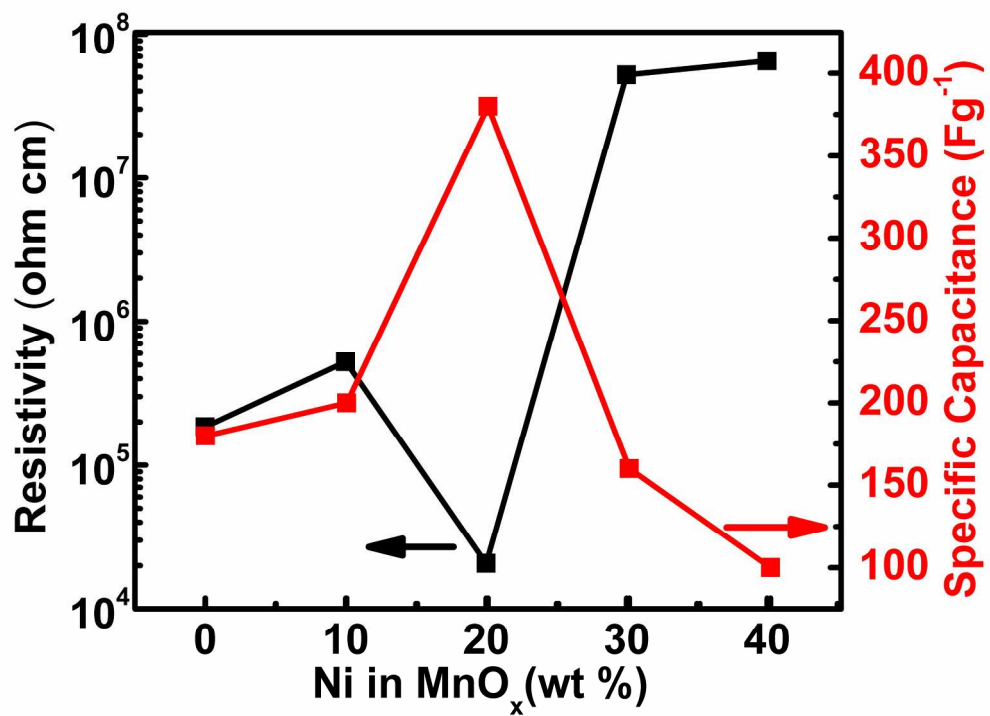
Sample Name	NiCl ₂ .6H ₂ O (g)	MnCl ₂ .4H ₂ O (g)	NaOH (g)	Ni/Mn (wt%)
Ni _{0.1} Mn _{0.9} O _x	0.48	3.56	1.60	10
Ni _{0.2} Mn _{0.8} O _x	0.95	3.16	1.60	25
Ni _{0.3} Mn _{0.7} O _x	1.43	2.77	1.60	43
Ni _{0.4} Mn _{0.6} O _x	1.90	2.37	1.60	65

Legend for Graphical abstract

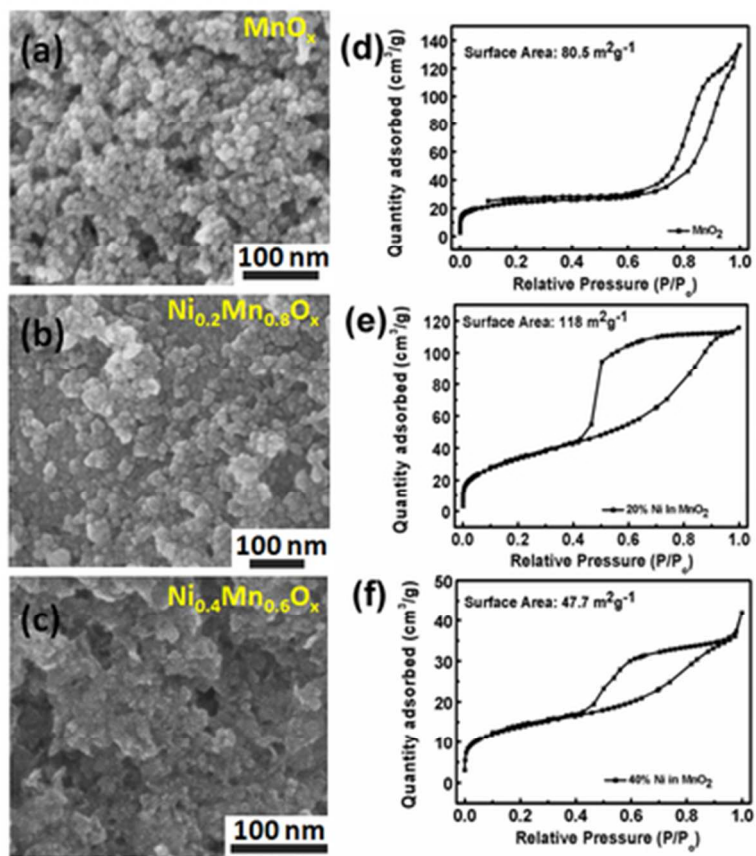
At optimised composition (20 wt %) of nickel, composite crystallizes into spinel NiMn_2O_4 that in a supercapacitor cell gives the best performance in terms of Energy and Power density.



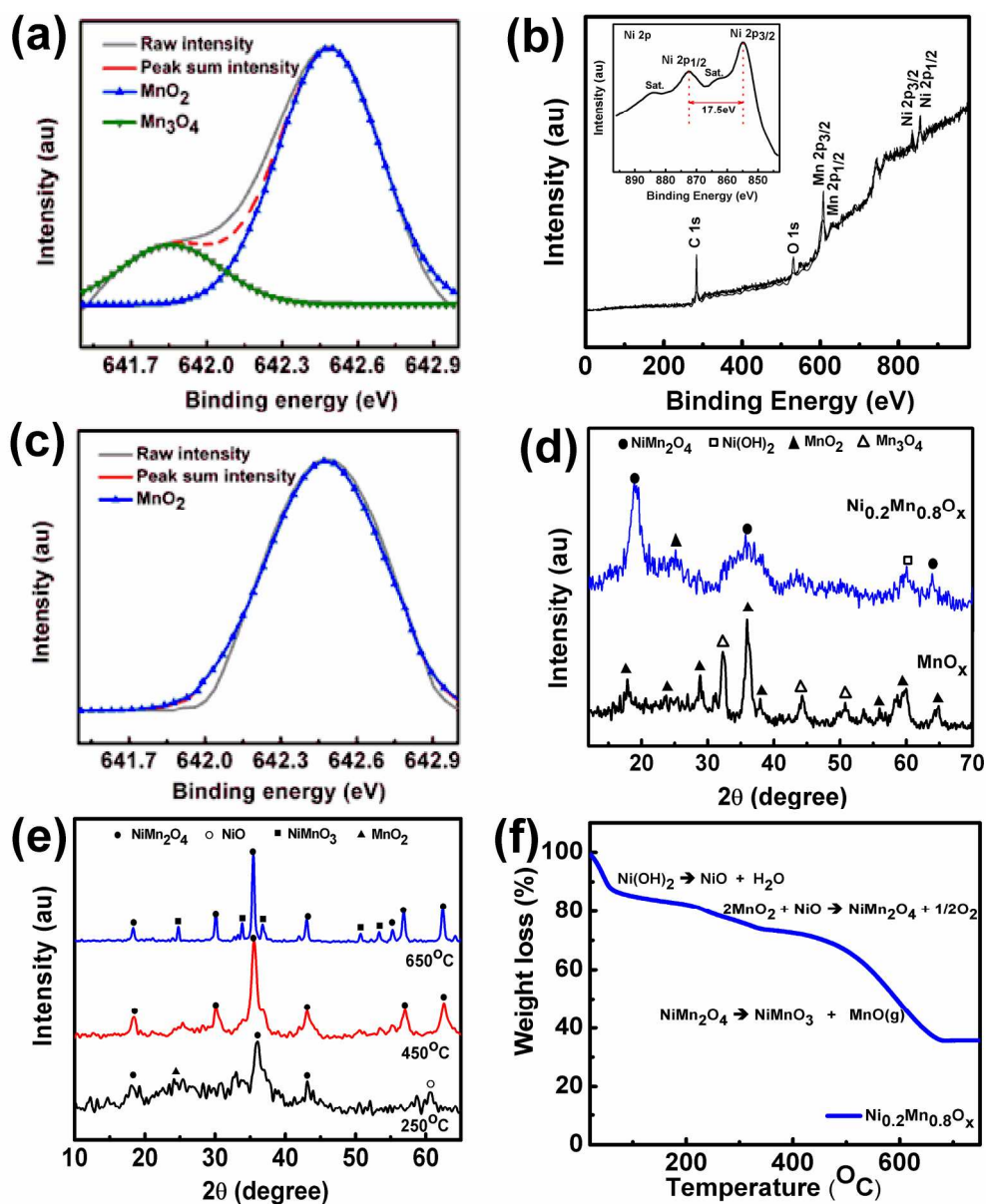
At optimised composition (20 wt %) of nickel, composite crystallizes into spinel NiMn₂O₄ that in a supercapacitor cell gives the best performance in terms of Energy and Power density.
23x13mm (300 x 300 DPI)



Effect of Ni (wt%) on resistivity and CSP of $Ni_yMn_{1-y}O_x$; $0 \leq y \leq 0.4$.
221x170mm (300 x 300 DPI)

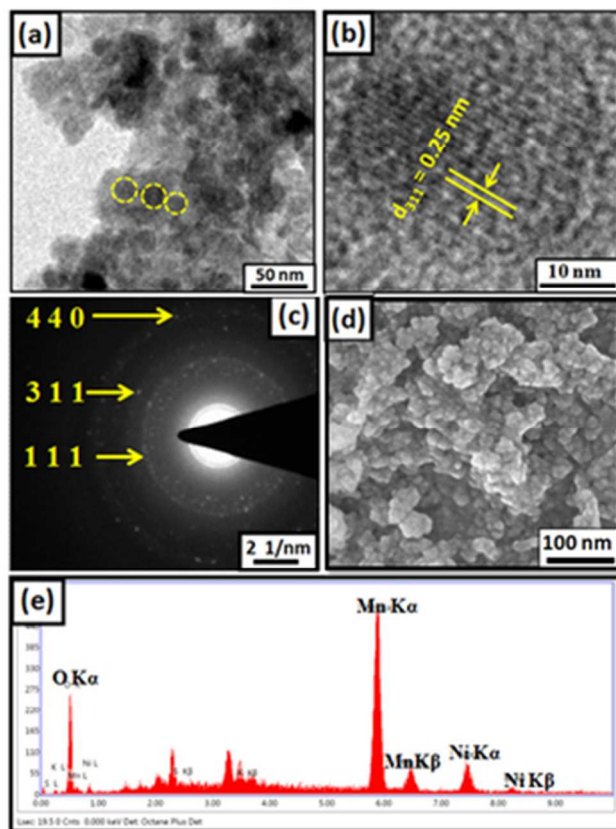


SEM micrographs (a, b and c) and N₂ adsorption-desorption isotherms (d, e and f) of MnO_x, Ni_{0.2}Mn_{0.8}O_x and Ni_{0.4}Mn_{0.6}O_x.
32x36mm (300 x 300 DPI)

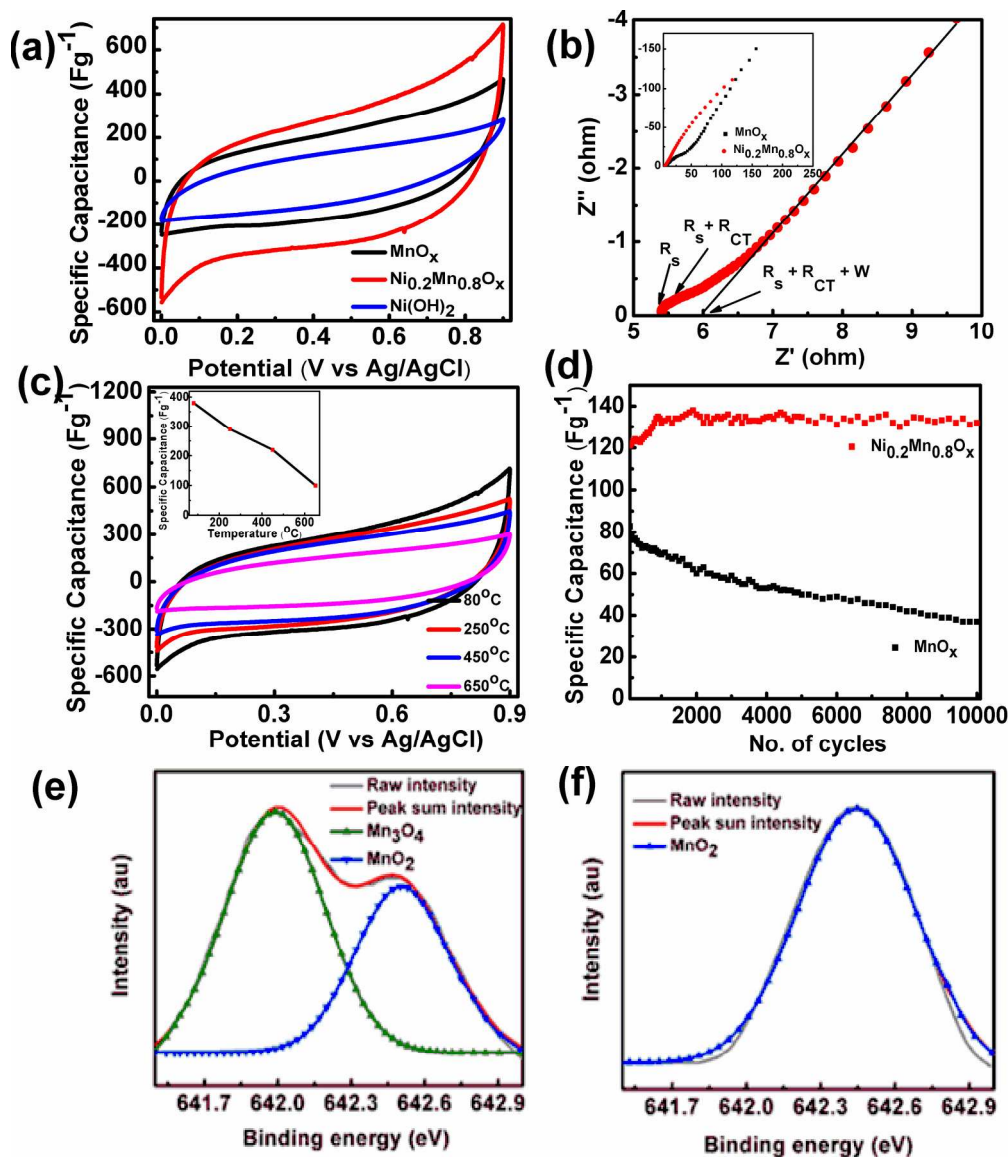


(a) Mn 2p X-ray photoelectron spectrum (XPS) of MnOx, (b) XPS survey scan with Ni 2p core level spectra in inset (c) Deconvoluted Mn 2p spectrum of Ni_{0.2}Mn_{0.8}O_x, (d) X-ray diffraction patterns of MnOx and Ni_{0.2}Mn_{0.8}O_x, (e) XRD patterns of Ni_{0.2}Mn_{0.8}O_x powder annealed at 250°C, 450°C and 650°C and (f) Thermogravimetric analysis of Ni_{0.2}Mn_{0.8}O_x.

202x241mm (300 x 300 DPI)

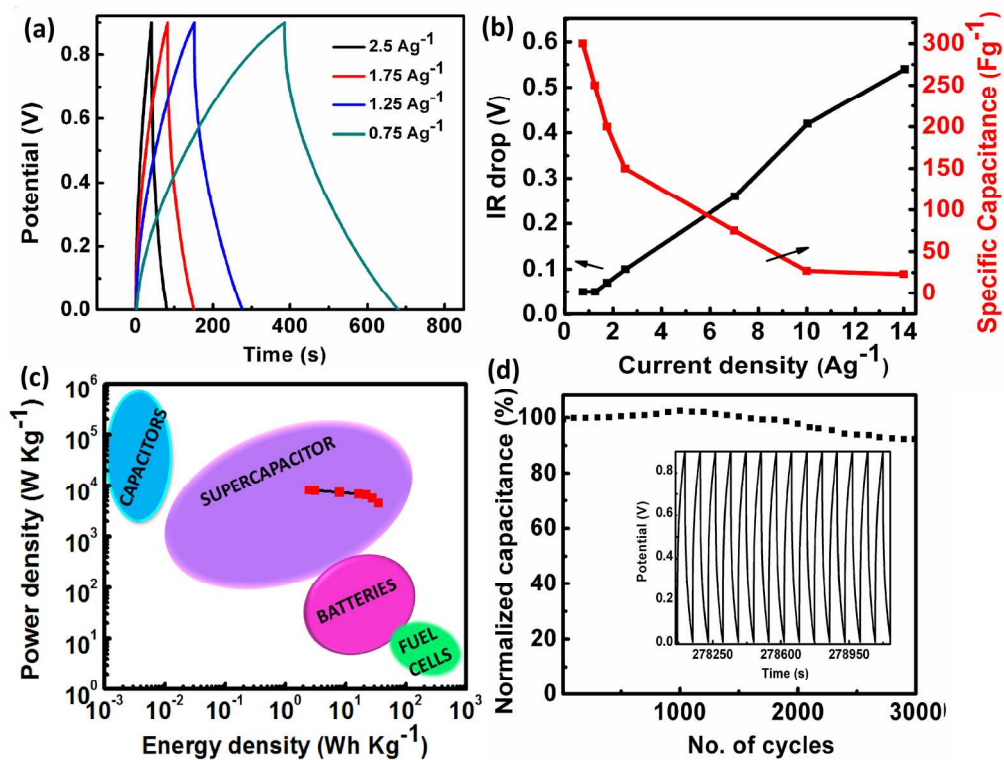


(a) TEM of $\text{Ni}_{0.2}\text{Mn}_{0.8}\text{O}_x$ and (b) HRTEM shows d spacing $\sim 0.25 \text{ nm}$, (c) SAED pattern, (d) SEM and (e) EDX of $\text{Ni}_{0.2}\text{Mn}_{0.8}\text{O}_x$ with atomic percentage of Ni:Mn ~ 0.25 .
28x35mm (300 x 300 DPI)



(a) Cyclic Voltammograms (CV) of MnO_x , Ni(OH)_2 and $\text{Ni}_{0.2}\text{Mn}_{0.8}\text{O}_x$ at 5mVs^{-1} , (b) Nyquist plot of $\text{Ni}_{0.2}\text{Mn}_{0.8}\text{O}_x$ in high frequency region. Inset shows Nyquist plot of MnO_x and $\text{Ni}_{0.2}\text{Mn}_{0.8}\text{O}_x$, (c) Effect of annealing temperature on CV response of $\text{Ni}_{0.2}\text{Mn}_{0.8}\text{O}_x$ electrode. Inset shows variation of specific capacitance vs annealed temperatures, (d) Cycling life test of MnO_x and $\text{Ni}_{0.2}\text{Mn}_{0.8}\text{O}_x$ at 50mVs^{-1} and (e and f) Mn 2p XPS spectra of $\text{Ni}_{0.2}\text{Mn}_{0.8}\text{O}_x$ and MnO_x after 10,000 CV cycles.

202x231mm (300 x 300 DPI)



(a) Galvanostatic charge discharge (GCD) curves at different current densities, (b) Variation of IR drop and specific capacitance vs current density, (c) Ragone plot and (d) GCD cycling performance of $\text{Ni}_0.2\text{Mn}_0.8\text{O}_x//\text{Ni}_0.2\text{Mn}_0.8\text{O}_x$ supercapacitor cell. Inset shows overview of last cycles. 183x141mm (300 x 300 DPI)